2022 19th International Conference on Electrical Engineering, Computing Science and Automatic Control (CCE). Mexico City, Mexico. November 9-11, 2022

FeOOH, α-Fe_2O_3, and $ZnFe_2O_4$ Thin Films Grown by Electrodeposition Method: Study for Photoanode Development

Rocío M. Sánchez-Albores, Instituto de Investigación e Innovación en Energías Renovables (IIIER-UNICACH), Chiapas, México magdalena.sanchez@unach.mx

Odín Reyes-Vallejo, Sección de Electrónica de Estado Sólido- Ingeniería eléctrica (SEES), CINVESTAV- IPN, Ciudad de México, México odin.reyes.v@cinvestav.mx

Arturo Fernández-Madrigal, Instituto de Energías Renovables-UNAM (IER-UNAM), Morelos, México afm@ier.unam.mx

Edna Ríos- Valdovinos, Instituto de Investigación e Innovación en Energías Renovables (IIIER-UNICACH), Chiapas, México edna.rios@unicach.mx

F. Pola-Albores, Instituto de Investigación e Innovación en Energías Renovables (IIIER-UNICACH), Chiapas, México, francisco.pola@unicach.mx

J. Moreira-Acosta, Laboratorio de Investigación, Universidad del Valle de México, Tuxtla Gutiérrez, 29056, Chiapas, México, jmoreira23@yahoo.com.mx

C.A. Meza-Avendaño, Instituto de Investigación e Innovación en Energías Renovables (IIIER-UNICACH), Chiapas, México carlos.meza@unicach.mx

ABSTRACT

This work presents the development of a photoanode for oxygen evolution reaction (OER). The deposit of FeOOH precursor film was performed by electrodeposition on FTO substrates varying the deposition charge. The FeOOH electrodes were heated at 500°C for 2 hours with a ramp of 2°C/min to obtain α-Fe_2O_3 films. Some of these FeOOH films were coated with a solution containing Zn^{+2} ions that, when heated, reacted to form $ZnFe_2O_4$. X-ray diffraction showed the formation of crystalline phases of each of these materials. As the thickness increases, the absorption edges of each material increase. Very similar morphologies are observed in the form of nanosheets in each of the samples. On the other hand, during the electrochemical characterization n-type behavior was observed. It is also observed that iron oxyhydroxides show electrocatalytic performance for OER with a starting potential at 1.2 V. Photocurrent measurements reveal that α-Fe_2O_3 is the most stable of the 3 materials, $ZnFe_2O_4$ also presents a photocurrent, however, it presents problems of recombination of photogenerated carriers. In general, these results show the potential use of α-Fe_2O_3 and $ZnFe_2O_4$ as photoanodes for water oxidation, however, together with other materials they can increase redox yields.

Keywords—*$ZnFe_2O_4$, FeOOH, Fe_2O_3, Electrodeposition, Photoelectrochemical water splitting, and OER.*

I. INTRODUCTION

Oxides based on iron have taken great interest due to their various applications, and in recent years there have been studies on their use in oxidation-reduction reactions for the splitting of the water molecule. Materials such as FeOOH (iron oxyhydroxide), Fe_2O_3 (hematite), and $ZnFe_2O_4$ (zinc ferrite) have been used to improve the photocatalytic activity of various materials since each one presents interesting properties. FeOOH works as a charge transfer mediator, in addition to acting as an efficient electrochemical catalyst for the oxygen evolution reaction (OER) [1] and serving as a passivating layer on the surface of some semiconductors such as $BiVO_4$ according to studies done by Araújo *et al* (2017) [2]. On the other hand, hematite has certain advantages such as having good stability, an adequate band gap (≈2.1 eV) that allows using part of the visible light of the solar spectrum, and a position of the edge of the band of valence that allows enough overpotential for the oxidation of water to O_2, in addition to being a non-toxic material and having a high theoretical value of photocurrent around 12.5 mA/cm^2 and 15.8% solar to hydrogen (STH) conversion efficiency [3]. Uniquely, ferrite has also emerged as a promising photoanode for the photoelectrolysis of water since it has a band gap close to ≈2 eV that is comparable to the α-Fe_2O_3 and it is also chemically and photochemically stable in basic media, has a conduction band edge very close to the hydrogen evolution potential [4]. These materials have been synthesized with various methods such as hydrothermal [5], chemical bath, immersion coating [6], and electrodeposition, this last method allows the growth of the semiconductor and metallic crystals directly from a conductive substrate with a good electrical contact, which can be easily integrated into devices [7]. The aim of this investigation is to study the role of FeOOH, Fe_2O_3, and $ZnFe_2O_4$ thin films as photoanodes in the splitting of the water molecule and to evaluate the structural, optical, morphological, and photoelectrochemical properties of these materials deposited by the electrodeposition method.

978-1-6654-5508-4/22/$31.00 ©2022 IEEE

II. EXPERIMENTAL SECTION

A three-electrode system and a BioLogic potentiostat VSP-300 were used for the electrodeposition of the films. The system had a working electrode (WE) (FTO glass), a reference electrode (REF) Ag/AgCl (KCl sat), and a platinum sheet as a counter electrode (CE).

For the FeOOH film deposit, a solution of $FeCl_2.5H_2O$ at 0.02M in 100mL of distilled water was prepared, then a compound agent $C_2H_3NaO_2$ (Sodium acetate) at 0.08 M was added, and it was placed in an ultrasonic bath for 15 min until achieve a homogeneous solution, then the solution was heated to 75 °C and kept stirred during the deposition process. An anodic deposition (oxidation of Fe^{+2} to Fe^{+3}, followed by precipitation of Fe^{+3} as FeOOH films) was performed at 1.2 V passing different charges of 50-100-250 mC, and the deposition of a light yellow material was observed. Finally, it was washed with distilled water and dried. To prepare Fe_2O_3 (hematite) films, the precursor films (FeOOH) obtained previously were calcined for 2 hours at 500 °C with a ramp of 2 °C/min. For the preparation of $ZnFe_2O_4$ films, drops of $Zn(NO_3)_2$ of 60 mM was added to cover all precursor electrode (FeOH), then it was calcined at 500 °C for 2 hours in presence of air, with a ramp of 2°C/min, then it was immersed in NaOH at 0.5 M for 15 minutes, and finally placed in an ultrasonic bath and then washed with deionized water to remove waste (ZnO) and purify the $ZnFe_2O_4$ phase.

III. CHARACTERIZATION

The crystal structures of the samples were examined by X-ray diffraction (XRD), using a Rigaku Ultima IV diffractometer with Cu Kα = 1.5418 Å radiation set at 40 kV and 40 mA in the 2θ range of 10–70° with a scanning speed of 0.2°/min. The Williamson-Hall method was used to calculate the crystal sizes and lattice micro-strain was obtained by X-ray peak broadening analysis.

An instrumental correction was performed with a standard pattern with Equation 1:

$$\beta_{hkl} = \left[\beta_{hkl\ measured}{}^2 - \beta_{hkl\ instrumental}{}^2\right]^{1/2} \quad (1)$$

Crystal size was calculated using Equation 2.

$$\beta_{hkl cos\theta} = \frac{k\lambda}{D} + 4\varepsilon sin\theta \quad (2)$$

Where β_{hkl} is the instrumental broadening, k is the shape factor (0.9), λ is a wavelength of Cuk_α radiation, D is crystal size, ε is the microstrain . The dislocation density (δ) was calculated using Equation 3

$$\delta = \frac{1}{D^2} \quad (3)$$

The morphology of the samples was observed using a Hitachi S-5500 Scanning Electron Microscope (SEM) operated at 5 kV. Topography analysis of thin films was performed using a Park Systems XE7 Atomic Force Microscope (AFM) in tapping mode with a scanned area of 5 x 5 μm^2 and 256 pixels; the thicknesses of the films were measured with a profilometer (needle profilometer model XP-200).UV-vis spectra were recorded with a Shimadzu model UV-3101 PC spectrophotometer in the spectral range of 250 to 1500 nm.

The absorption coefficient was calculated by Equation 4[8] using the T and R values:

$$\alpha(\lambda) = \frac{1}{d} ln\left[\frac{(1-R)^2}{2T} + \sqrt{\frac{(1-R)^4}{4T^2} + R^2}\right] \quad (4)$$

where d is the thickness of the films. In semiconductors, the absorption coefficient is related to hν (Energy) according to Equation 5 [9]:

$$\alpha = A\frac{(hv-Eg)^{\frac{1}{n}}}{hv} \quad (5)$$

where A is constant, hv is the photon energy, and n is 2 or 1/2 for direct or indirect allowed transitions, respectively [10]. The Urbach energy (E_U) was estimated by equation 6 [11].

$$\ln(\alpha) = \ln(\alpha_0) + \left(\frac{hv}{E_U}\right) \quad (6)$$

Electrochemical measurements were performed in an aqueous solution of Na_2SO_4 (0.5 M), which was used as an inert electrolyte (pH 7), and using a 3-electrode configuration: a platinum counter electrode, an Ag/AgCl (sat) reference electrode, and a working electrode (as studio films). The electrochemical impedance was measured in dark conditions using a frequency of 15 kHz, the applied potential was varied from -0.8 to 1 V (Ag/AgCl), with an amplitude of 25 mV which was carried out to measure the flat band potential (E_{FB}). According to on the depletion layer model, the capacitance of the semiconductor space charge layer (CSC) depends on the applied potential (V) and can be described using by the Mott-Schottky equation 7 [12]:

$$\frac{1}{C^2} = \frac{2}{\varepsilon\varepsilon_0 A^2 e N_d}\left(V - E_{FB} - \frac{k_B T}{e}\right) \quad (7)$$

where C is the space charge capacity (capacitance) (F); A is the active geometric area (cm^2), ε is the relative dielectric constant of material (FeOOH is11 F m^{-1}, [13];α-Fe_2O_3 is 80 F m^{-1}, [14]; and $ZnFe_20_4$ is 54 F m^{-1},[15]; ε_0 is the vacuum permittivity (8.854×10^{-12} F m^{-1}); N_d is the donor density (cm^{-3}), e is the electron charge (1.602×10^{-19} C); V is the applied potential referenced to a reversible hydrogen electrode (RHE); k_B is the Boltzmann constant (1.381×10^{-23} JK^{-1}) and T is the absolute temperature (298 K). The flat band potential (E_{FB}) is determined by finding the x-intercept of the linear fitting in the Mott-Schottky plot, $1/C^2$ as a function of the applied potential (E). N_d was estimated from the slope of the Mott-Schottky plot, Equation 8:

$$Nd = \frac{2}{\epsilon_0 \epsilon\, e_0}\left[\frac{d\left(\frac{1}{C^2}\right)}{dV_s}\right]^{-1} \quad (8)$$

Photocurrent curves were recorded in the anodic direction in a potential range from of -0.3 to 1 V (Ag/AgCl), using a 50 W JDR halogen lamp as a light source and calibrated to achieve AM 1.5G conditions.

IV. RESULTS

Fig. 1a presents the FeOOH diffraction patterns obtained at 50, 100, and 250 mC. It is observed that in all samples the FeOOH phase indexed to the orthorhombic is formed according to the (PFD No 01078-8774) with characteristic peaks in the planes of (110), (211), (220), and (002) corresponding to 2θ= 26.46°, 51.55°,54.68°, and 61.69° respectively. It can be seen that with the increase in the load of the deposition there is a decrease in the intensity of diffracted peaks corresponding to FeOOH, no significant change in crystal size is observed, but a decrease in microstrain and density of dislocation (Table 1), which is indicative of the passivation of the defects. Fig. 1b shows the characteristic peaks in the planes (012), (104), (111), (113), (024), and (116) of the α-Fe_2O_3 hematite phase (PDF No. 01–089-0599), and they are similar to those reported in other investigations [16], it is also observed that with the increase of the charge there is a decrease in the micro-strain and dislocation density this is attributed to the decrease in defect levels due to the increase in the size of the crystallite size.[17].

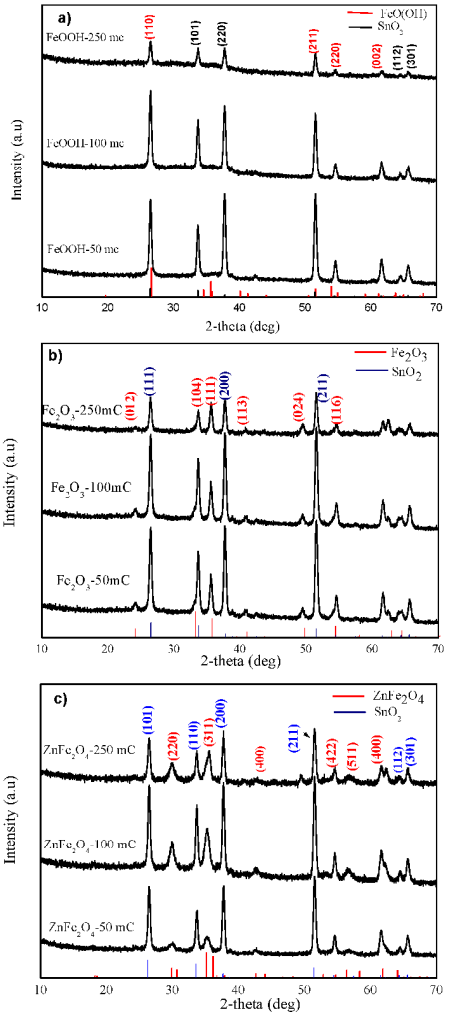

Fig. 1. XRD spectra of a)FeOOH, b)α-Fe_2O_3, and c)$ZnFe_2O_4$ thin films deposited

In fig. 1c the sharp peaks of the planes at (220), (311), (400), (422),(511), and (440) correspond to the cubic spinel $ZnFe_2O_4$ phase (PDF No. 01-070-6493). Also, micro-strain reduces as the charge increases which is related to a decrease in disorder (Measured as Urbach energy), these data are comparable with the patterns observed in other investigations such as that obtained by Reddy *et al* [18].

Table 1 shows the band gap values of FeOOH and they were estimated at 1.83 to1.85 eV, despite the increase of thickness, these values remain constant and are similar to those observed in other investigations [19]. The Fe_20_3 the band gap values of 1.84, 1.87, and 1.88, assuming an indirect transition for both cases [20]. The values obtained of the band gap of $ZnFe_2O_4$ calculated are 1.75, 1.80, and 1.96 eV, and are similar to those reported in other investigations [18]. This increment in E_g with the increase of thickness is associated with the reduction of strain, the increase of crystallite size, and the decrease in structural disorder (E_U) since there are fewer localized states between the gap (valence and conduction band), and it is known that the penetration of the Urbach tail in the forbidden region depends on the number of defects, which coincides with the variations of micro deformations presented in table 1 [8][21].

Table 1: Structural parameters: D= crystal size, Eg=Band gap, t= thickness, ϵ=micro-strain and R= Roughness

Sample	*D* (nm)	*ϵ*	*δ* (10^{-3} nm^{-2})	t (nm)	*Eg* (eV)	*Eu* (mV)	*R* (nm)
FeOOH 50 mC	11.38	5.88 x10^{-4}	7.72	297	1.83	357.1	15.37
FeOOH 100 mC	11.68	3.54 x10^{-4}	7.31	709	1.84	320.9	20.48
FeOOH 250 mC	12.10	2.21 x10^{-4}	6.8	1165	1.85	298.3	18.33
Fe_2O_3 50 mC	14.36	2.67 x10^{-3}	4.84	307	1.84	172.4	40.48
Fe_2O_3 100 mC	15.35	2.03 x10^{-3}	4.24	625	1.87	171.2	23.91
Fe_2O_3 250 mC	18.76	1.05 x10^{-3}	2.84	1100	1.88	145.8	41.52
$ZnFe_2O_4$ 50 mC	11.05	7.17 x10^{-3}	8.1	471	1.75	458.5	15.3
$ZnFe_2O_4$ 100 mC	10.75	6.15 x10^{-3}	8.6	738	1.80	356.9	29.03
$ZnFe_2O_4$ 250 mC	11.75	3.22 x10^{-3}	7.2	1287	1.96	150.1	17.86

Figs. 2 a, b, and c show the morphology of the FeOOH thin films. Particles in the form of dense nanosheets with very narrow thicknesses are observed that grow vertically to the FTO substrate in the form of an interconnected network. This structure presents free spaces between the sheets of the layers. As the deposited charge increases, it is observed that the nanosheets are interconnected in the form of flower petals. The increase in this porous architecture improves conductivity, favoring the transfer of charge. It can be observed in figure 4a with the FeOOH sample treated at 250 mC presenting a greater electrocatalytic response. Similar morphologies have been observed in the research of Shen *et al,* [22]. The morphology of the hematite films is presented in the figs. 2d, e, and f, greater growth of the particles and better distribution are observed as the charge increases. These changes can also be seen in the AFM images in figs. 3d, e, and f. The FE-SEM images of the $ZnFe_2O_4$ films are presented in figures 2g, h, and i. The first two conditions promote a smooth appearance which is related to the

greater amount of ZnO removed during the NaOH etching process, while when the charge was 250 mC less ZnO is formed due to more Fe precursor is available for the formation of $ZnFe_2O_4$ phase, consequently, less ZnO is removed resulting in a roughness appearance. Also, it is confirmed in the AFM images in fig. 3g, h, and i, in which the most porous appearance is observed when 250 mC of FeOOH is deposited. These results are in agreement with the crystallite sizes, calculating the smallest values when 50 and 100 mC of FeOOH is deposited.

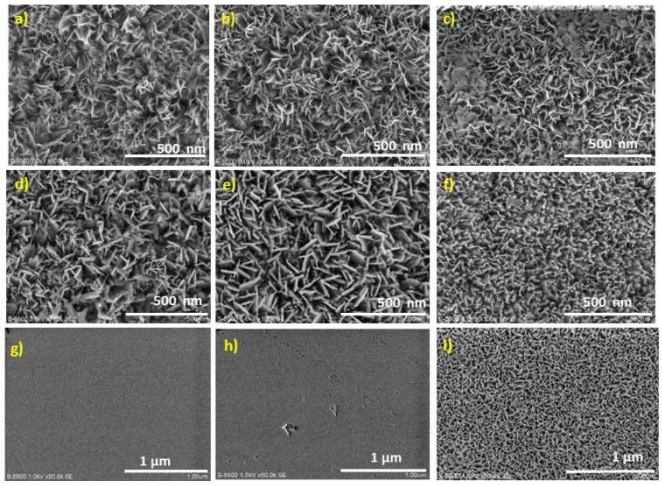

Fig. 2. : FE-SEM images of thin films deposited on FTO substrates: a) FeOOH-50 mC, b) FeOOH-100 mC, c) FeOOH-250 mC, d) Fe_2O_3-50 mC, e) Fe_2O_3-100 mC, f) Fe_2O_3-250 mC, g) $ZnFe_2O_4$-50 mC, h) $ZnFe_2O_4$-100 mC i) $ZnFe_2O_4$-250 mC.

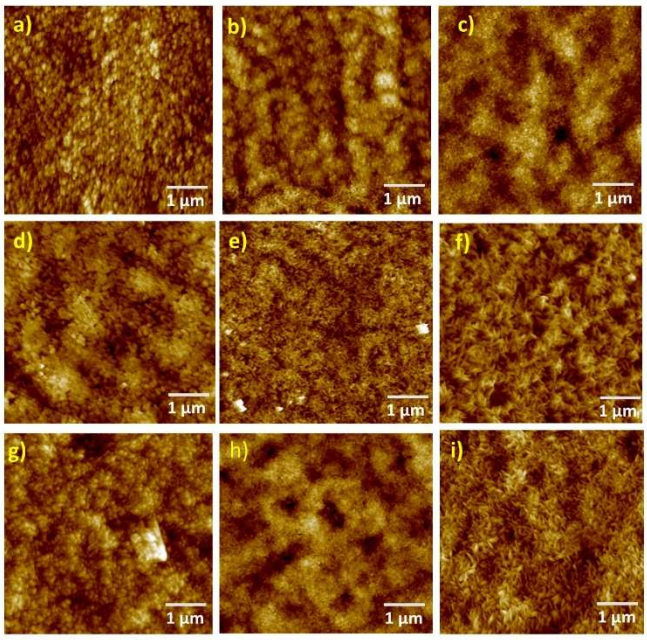

Fig. 3. AFM images of thin films deposited on FTO substrates: a) FeOOH-50 mC, b) FeOOH-100 mC, c) FeOOH-250 mC, d) Fe_2O_3-50 mC, e) Fe_2O_3-100 mC, f) Fe_2O_3-250 mC, g) $ZnFe_2O_4$-50 mC, h) $ZnFe_2O_4$-100 mC i) $ZnFe_2O_4$-250 mC.

Fig. 4a shows the photoresponse graphs of the FeOOH thin films deposited on FTO applying charges of 50, 100, and 250 mC. It is observed that there is no generation of photocurrent since FeOOH is a material that acts as a transfer mediator center of charge center and not as a catalyst by itself, this hypothesis has been supported by an absence of change in the starting potential, without photocurrent saturation, as has been shown in other investigations [2, 23]. A starting potential at 1.2V is observed for the simples obtained at 250 and 100 mC films and 1.35V for the sample deposited at 50 mC. An increase in anode current is also observed in all the samples, which suggests that they have a greater electrocatalytic capacity toward OER reactions[23, 24]. which is consistent with the decrease in the Urbach energy since its decrease promotes a decrease in conductivity, so thicker films are more resistive according to Reyes et al [8,25].

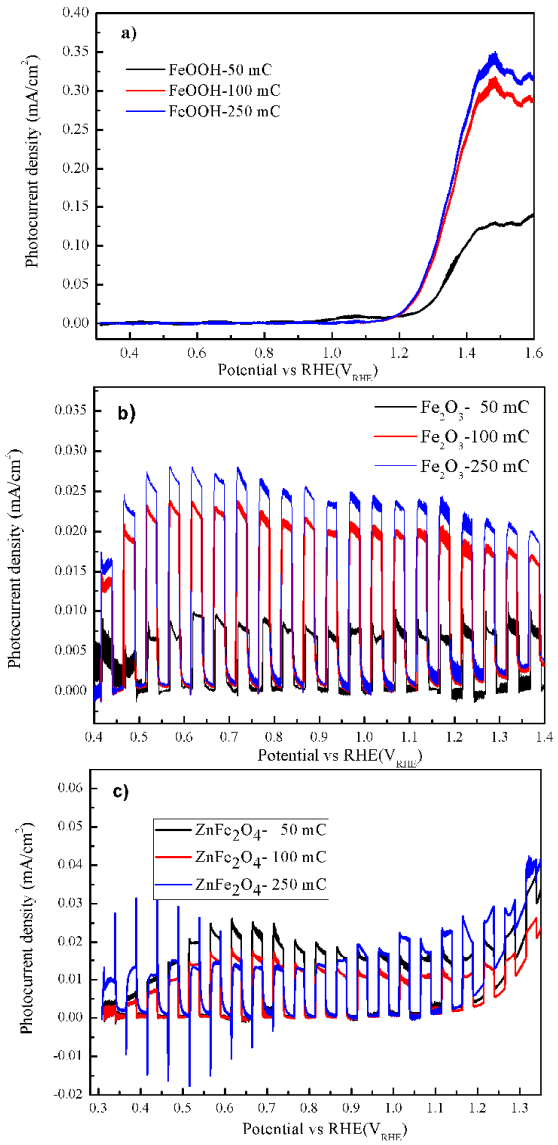

Fig. 4. Photocurrent of a) FeOOH, b) α-Fe_2O_3, and c) $ZnFe_2O_4$ thin films deposited.

In Fig. 4b it is observed that hematite is more stable since it has a starting potential at zero, the response to light is fast and after the initial peak the photocurrent decreases due to the recombination of holes and electrons (Transient currents). The sample treated at 250 mC presents a better response to the photocurrent, however, it is observed that at high potentials the photocurrent decreases. This may be due to the slow kinetics of the charge transfer as well as the high intrinsic resistance in these

iron oxides, which induces an additional degradation of the iron [26]. The N_d values obtained, listed in Table 2, are similar to those values reported for α-Fe_2O_3 thin films, which are in the order of 10^{18} cm^{-3}). Fig. 4c shows photocurrents of the $ZnFe_2O_4$ films with charges of 50,100 and 250 mC. The sample treated at 250 mC shows anodic current peaks that have their origin in the accumulation of holes in the electrode/electrolyte interface, these holes are not injected into the electrolyte and they are accumulated. On the contrary, the cathodic current peaks are generated when the illumination of the light is off, which denotes the recombination of the holes accumulated in the junction of the semiconductor with the electrons of the conduction band [14]. Films treated at 50 and 100 mC have shown reduced positive peaks, converging in less interfacial recombination and enhanced charge transfer, however, a low yield of spinel ferrite is observed, suggesting strong recombination of photogenerated charges.

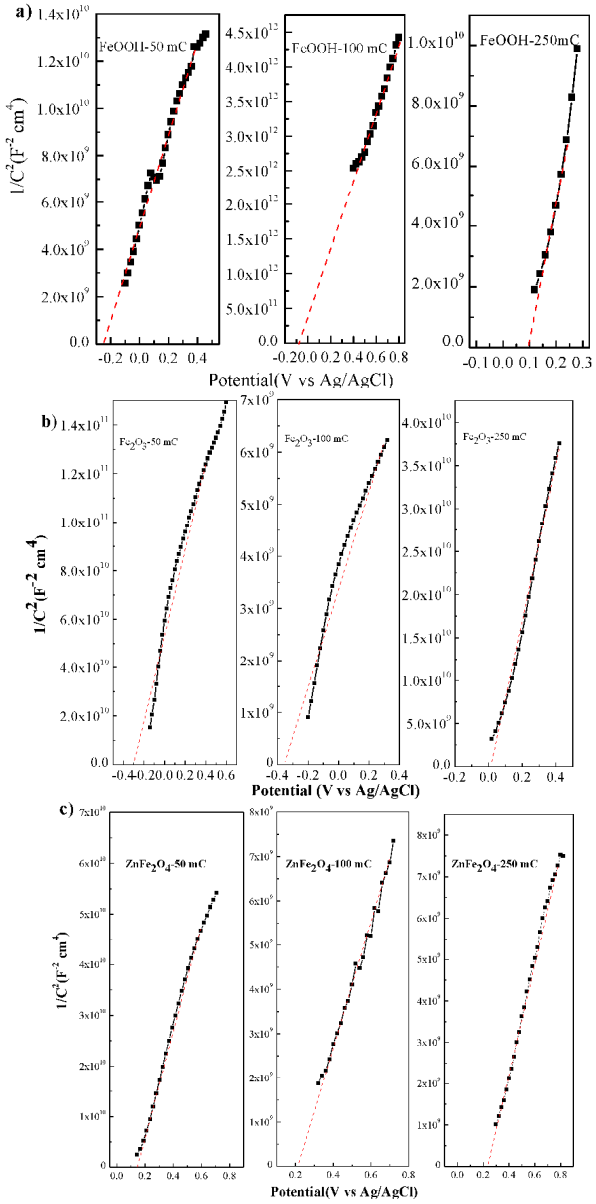

Fig. 5. Flat band potential of thin films deposited on FTO substrates a)FeOOH, b)Fe_2O_3, and c)$ZnFe_2O_4$

Table 2 Electrochemical parameters: E_{FB}= Flat band potential, and N_d= Carrier density.

Sample	E_{FB} (V vs Ag/AgCl)	E_{FB} (V vs NHE)	N_d (cm^{-3})
FeOOH 50 mC	-0.25	0.361	$6.64x10^{18}$
FeOOH 100 mC	-0.08	0.531	$2.59x10^{16}$
FeOOH 250 mC	0.09	0.701	$2.60x10^{16}$
Fe_2O_3 50 mC	-0.29	0.361	$9.91x10^{16}$
Fe_2O_3 100 mC	-0.35	0.261	$1.81x10^{18}$
Fe_2O_3 250 mC	0.01	0.621	$1.94x10^{17}$
$ZnFe_2O_4$ 50 mC	0.15	0.761	$2.90x10^{17}$
$ZnFe_2O_4$ 100 mC	0.22	0.831	$1.93x10^{18}$
$ZnFe_2O_4$ 250 mC	0.24	0.851	$1.89x10^{18}$

The flat band potential, E_{FB}, and carrier density are estimated from the x-axis interception of the linear fitting of the Mott-Schottky plot and its slope, respectively; these values are presented in Table 2. The positive slope in the MS plots confirms an n-type semiconductor behavior (Fig. 5). A shift to the positive side of the flat band potential is observed in all samples. The positive change of the flat band potential with respect to deposited charge suggests an increase in band edge bending that enhances charge separation by decreasing the recombination of holes and photogenerated electrons[27].

V. CONCLUSIONS:

Crystalline films of FeOOH, α-Fe_2O_3, and $ZnFe_2O_4$ were deposited on FTO substrates using the electrodeposition method. FeOOH films exhibited high activity towards oxygen evolution reactions, being the sample deposited at 250 mC was the one with the highest electrocatalytic activity, however, there is no generation of photocurrent since FeOOH is an oxide that acts as a mediation center for charge transfer and not as a catalyst. On the other hand, hematite is a material that presents greater stability in an aqueous environment under typical study conditions, it has a small band gap (1.84-1.88 eV) which favors the absorption of light. However, due to the intrinsic resistance, there was a decrease in the photoresponse due to the slow charge transfer capacity. Zinc ferrite presents a greater instability due to the formation of peaks in cathodic and anodic currents, which is due to recombination of photogenerated charges, and at high potentials, it was favored towards OER reactions. All the thin films exhibited n-type behavior according to the Mott-Schottky plots. These results open the possibility of investigating the combination with other materials to increase the yields in redox reactions.

VI DECLARATION OF COMPETING INTEREST

The authors declare that they have no known competing financial interests or personal relationships that could have appeared to influence the work reported in this paper

VII ACKNOWLEDGMENT:

R. Sánchez-Albores and Odín Reyes-Vallejo, acknowledge CONACYT for the doctoral and postdoctoral fellowships respectively to carry out the present work. The authors acknowledge the technical support received from Ing. Oscar Gómez Daza, and MSc Alejandra García-Sotelo for general assistance, Dr. Patricia Altuzar Coello and MSc María Luisa Ramón García for XRD analysis, and Rogelio Morán Elvira for SEM images.

VIII REFERENCES:

[1] Y. Sakamoto, Y. Noda, K. Ohno, K. Koike, K. Fujii, T.M. Suzuki, T. Morikawa, and S. Nakamura, "First principles calculations of surface dependent electronic structures: a study on β-FeOOH and γ-FeOOH," Phys. Chem. Chem. Phys., vol. 21, pp. 18486-18494, 2019.

[2] M.A. de Araujo, D. Coelho, L.H Mascaro, and E.C. Pereira, "The iron oxyhydroxide role in the mediation of charge transfer for water splitting using bismuth vanadate photoanodes, " J Solid State Electrochem., vol. 22, pp. 1539–1548, 2018.

[3] A.G. Tamirat, J. Rick, A.A. Dubale, W-N. Su, and B.J. Hwang, "Using hematite for photoelectrochemical water splitting: a review of current progress and challenges," Nanoscale Horiz., vol.1, pp. 243-267, 2016.

[4] K.J. McDonald and K-S. Choi, "Synthesis and Photoelectrochemical Properties of $Fe_2O_3/ZnFe_2O_4$ Composite Photoanodes for Use in Solar Water Oxidation," Chem. Mater., 23, 21, pp. 4863–4869, 2011.

[5] Y. Wei, A. Liao, L. Wang, X. Wang, D. Wang, Y. Zhou, and Z. Zou, " Room Temperature Surface Modification of Ultrathin FeOOH Cocatalysts on Fe_2O_3 Photoanodes for High Photoelectrochemical Water Splitting," J. Nanomater., vol. 2020. ID 7148714, 2020.

[6] K. Kirchberg, S. Wang, L. Wang, and R. Marschall, "Mesoporous $ZnFe_2O_4$ Photoanodes with Template-Tailored Mesopores and Temperature-Dependent Photocurrents, " Chem Phys Chem., vol. 19 (18), pp. 2313-2320, 2018.

[7] S. Jiao, L. Xu, K. Hu, J. Li, S. Gao, and D. Xu, "Morphological Control of α-FeOOH Nanostructures by Electrodeposition," J. Phys. Chem. C, vol. 114, pp. 269-273, 2010.

[8] O. Reyes-Vallejo, R. Sánchez-Albores, A. Fernández-Madrigal, S. Torres-Arellano, and P.J. Sebastian, "Evaluation of hydrogen evolution reaction on chemical bath deposited Cu_2O thin films: Effect of copper source and triethanolamine content," Int. J. Hydrog. Energy, vol. 47 (54), pp. 22775-22786, 2022.

[9] S. J. Ikhmayies, R.N, Ahmad-Bitar, "A study of the optical bandgap energy and Urbach tail of spray-deposited CdS:In thin films," J. Mater. Res. Technol., vol. 2 (3), pp. 221-227, 2013.

[10] T.G. Sánchez, X. Mathew, and N.R. Mathews, "Obtaining phase-pure CZTS thin films by annealing vacuum evaporated CuS/SnS/ZnS stack," J. Cryst. Growth, vol. 445, pp. 15-23, 2016.

[11] F. Urbach, "The Long-Wavelength Edge of Photographic Sensitivity and the Electronic Absorption of Solids," Phys. Rev., 92 (5), 1324, 1953.

[12] S.P. Harrington, and T.M. Devine, "Analysis of Electrodes Displaying Frequency Dispersion in Mott-Schottky Tests," J. Electrochem. Soc., 155 (8), C381-C386, 2008.

[13] D. Chen, M. Yen, P. Lin, S. Groff, R. Lampo, M. McInerney, and J. Ryan, "A Corrosion Sensor for Monitoring the Early-Stage Environmental Corrosion of A36 Carbon Steel," Materials, 7(8), pp. 5746-5760, 2014.

[14] S. Emin, M. de Respinis, T. Mavric, B. Dam, M Valant, and W.A. Smith, "Photoelectrochemical water splitting with porous α-Fe_2O_3 thin films prepared from Fe/Fe-oxide nanoparticles," Appl. Catal. A-Gen., vol.523, pp. 130-138, 2016.

[15] V.V. Petrov, E.M. Bayan, V.Yu. Storozhenko, M.A. Bunin, Yu. N. Varzarev, A.V. Nesterenko, and I.V. Rybalchenko, "Structure and dielectric properties of thin nanocrystalline $ZnFe_2O_4$ films," Ferroelectrics, vol. 575 (1), pp. 130–139, 2021.

[16] S.S. Shinde, R.A. Bansode, C.H. Bhosale, and K.Y. Rajpure, "Physical properties of hematite α-Fe_2O_3 thin films: application to photoelectrochemical solar cell," J. Semicond, vol. 32, 2011.

[17] Z. Braiek, M. Gannouni, I.B. Assaker, A. Bardaoui, A. Lamouchi, A. Brayek, and R. Chtourou, "Correlation between physical properties and growth mechanism of In_2S_3 thin films fabricated by electrodeposition technique with different deposition times," Eur. Phys. J. Appl. Phys., vol. 72, 1032, 2015.

[18] I. Neelakanta Reddy, Ch. Venkata Reddy, A. Sreedhar, J. Shim, M. Cho, K. Yoo, D. Kim, and J. Seog Gwag, "A stable novel nanostructure of $ZnFe_2O_4$ based nanocomposite for improved photoelectrocatalytic and photocatalytic activities," J. Electroanal Chem., vol. 823, pp. 517-526, 2018.

[19] H. Zhang, M. Bayne, S. Fernando, B. Legg, M. Zhu, R. Lee Penn, and J. F. Banfield, "Size-Dependent Bandgap of Nanogoethite", J. Phys. Chem. C, vol. 115 (36), pp. 17704-17710, 2011.

[20] G. Wang, Y. Ling, and Y. Li, "Oxygen-deficient metal oxidenanostructures for photoelectrochemical water oxidation and other applications," Nanoscale, vol. 4 (21), pp. 6682-6691, 2012.

[21] J. Singh, S. Sharma, S. Sharma, R. C.Singh, " Effect of tungsten doping on structural and optical properties of rutile TiO2 and band gap narrowing" Optik,vol 186,p.p 538-547,2019

[22] B. Shen, R. Guo, J. Lang, L. Liu, L. Liu, and X. Yan, "High-Temperature Flexible Supercapacitor Based on Pseudocapacitive Behavior of FeOOH in Ionic Liquid Electrolyte," J. Mater. Chem. A, vol. 4 (21), pp. 8316-8327, 2016.

[23] X. Zhang, L. An, J. Yin, P. Xi, Z. Zheng, and Y. Du, "Effective Construction of High-quality Iron Oxy-hydroxides and Co-doped Iron Oxy-hydroxides Nanostructures: Towards the Promising Oxygen Evolution Reaction Application," Sci Rep., vol. 7, 43590, 2017.

[24] F.N.I. Sari, S. Abdillah, and J-M. Ting, "FeOOH-containing hydrated layered iron vanadate electrocatalyst for superior oxygen evolution reaction and efficient water splitting," Chem. Eng. J., vol. 416, 129165, 2021.

[25] Reyes-Vallejo, O., Escorcia-García, J., & Sebastian, P. J. (2022). Effect of complexing agent and deposition time on structural, morphological, optical and electrical properties of cuprous oxide thin films prepared by chemical bath deposition. Materials Science in Semiconductor Processing, 138, 106242.

[26] J. Wang, L. Li, C. L. Wong, L. Sun, Z. Shen, and S. Madhavi, "Controlled synthesis of α-FeOOH nanorods and their transformation to mesoporous α-Fe_2O_3, Fe_3O_4@C nanorods as anodes for lithium ion batteries," RSC Adv., vol. 3 (35), pp. 15316-15326, 2013.

[27] M. Huang, J. Bian, W. Xiong, C. Huang, and R. Zhang, "Low-dimensional Mo:$BiVO_4$ photoanodes for enhanced photoelectrochemical activity," J. Mater. Chem. A, vol.6, pp. 3602-3609, 2018.